Acta Crystallographica Section A
Foundations of Crystallography
ISSN 0108-7673

Received 23 April 2002
Accepted 3 September 2002

© 2002 International Union of Crystallography
Printed in Great Britain – all rights reserved

Kinematic and dynamical CBED for solving thin organic films at low temperature; experimental tests with anthracene

J. S. Wu and J. C. H. Spence*

Department of Physics and Astronomy, Arizona State University, Tempe, AZ 85287-1504, USA. Correspondence e-mail: spence@asu.edu

Low-dose, low-temperature kinematic and dynamical convergent-beam electron diffraction (CBED) patterns from thin organic crystalline films have been used for the measurement of structure-factor amplitudes and phases. Kinematic conditions are identified by the observation of uniform intensity within the CBED discs and used to determine structure-factor magnitudes. CBED patterns from thicker regions affected by multiple scattering give structure-factor signs, which are varied for best fit. The use of a small probe (and the Kohler SAD mode) minimizes bending artifacts. A new method of thickness determination is evaluated. The approach is tested using experimental data from the centrosymmetric anthracene structure, the results compared with direct methods, and a potential map derived from experimental data. The faint peaks due to H-atom positions may be distinguished. Key issues influencing the validity of the method such as the appropriate dimension of the structure-factor matrix, sample thickness and crystal orientation are discussed.

1. Introduction

In previous work (Wu & Spence, 2002), we have shown that useful convergent-beam electron diffraction (CBED) patterns may be obtained from organic crystals at low temperature. For inorganic crystals, thickness variations and multiple scattering normally prevent the collection of reproducible transmission electron diffraction (TED) spot-pattern data, while, for non-biological thin organic films, bending and radiation damage have a similar effect. In this paper, we demonstrate the use of 'Kohler-mode' spot patterns and kinematic ('blank disc') CBED patterns from a thin centrosymmetric organic crystal (anthracene) for the determination of structure-factor magnitudes under kinematic conditions. While this approach may not be useful in biology (where large numbers of unit cells are needed to provide redundancy against radiation damage), however it does appear to be useful for the more radiation resistant, unsaturated, π-bonded aromatic hydrocarbon molecules. The observation of CBED discs of approximately uniform intensity (blank discs) is a useful experimental test for single-scattering conditions. The small illuminated area used by both methods minimizes bending effects. Data are recorded at liquid-nitrogen temperature to reduce radiation damage, and an elastic imaging filter is used to reduce background in the diffraction patterns. We then use CBED patterns from a thicker crystal, where multiple scattering is present, to determine the structure-factor phases. We base these calculations on the structure-factor magnitudes obtained from the thin areas and vary their signs (and thickness) for best fit to the dynamical CBED patterns. Because in centrosymmetric structures only the signs of the structure factors (to which the dynamical intensities are extremely sensitive) are varied, the number of possibilities is relatively small and multiparameter optimization is rapid. The results are compared with the application of direct methods to the kinematic data. We also evaluate a new method of thickness determination.

The multislice and Bloch-wave methods provide two well established methods for calculation of the intensity of reflections when an atomic structure is known. The direct inversion from observed multiply scattered intensities to the crystal potential has also been theoretically discussed for unknown structures, and several approaches suggested (Spence, 1998; Allen *et al.*, 1998). Methods based on the two-beam model for dynamical scattering and the approximation $|F_g| \sim I_g$ have been tested (Vainshtein, 1964; Cowley, 1992*a*,*b*; Wu & Spence, 2002). Although this approximation was previously used only for correcting electron diffraction data from mosaic crystals and polycrystalline specimens, Weirich *et al.* (2000) note that this type of correction also improves the quality of single-crystal data. However, the two-beam model has been shown to be inadequate at least for explaining how multiple scattering influences individual intensity (Dorset, 1995). While a two-beam approximation can be helpful for structure determination in some cases, the use of the Bloch-wave method includes as many beams as necessary to account for dynamical effects, and thus should be used for *ab initio* structure analysis.

Crystal thickness and orientation are two important parameters influencing the observed intensities of electron

diffraction. Thus, in the first part of this paper, we firstly discuss a method to estimate sample thickness (t) and orientation ($\mathbf{K}_t$) using a kinematical approximation that includes the excitation error. The estimated thickness can be used as an indication of deviations from the kinematical approximation.

There have been two main approaches to solving the phase problem of electron crystallography. Firstly, the phases of some reflections can be derived from high-resolution electron images. This has been demonstrated by Unwin & Henderson (1975) for biological specimens and by Klug (1978/79). The phases that are lost in diffraction patterns are preserved in the images and can be extracted from the Fourier transforms (DeRosier & Klug, 1968). However, beam-sensitive materials may be quickly destroyed under imaging conditions. The use of direct methods is the second approach to solving the phase problem if electron diffraction patterns can be taken from very thin areas, say less than 75 Å (Dorset *et al.*, 1979), so that the observed intensities can be treated kinematically (Dorset & Hauptman, 1976). It offers the big advantage for organic crystals that the electron density can be reduced by 100 times or more that used for imaging. Recently, the structures of several unknown compounds including ceramic oxides (Sinkler *et al.*, 1998) and a precipitate Al_mFe in aluminium alloys (Gjønnes *et al.*, 1998) have been solved using electron diffraction data. Direct methods have also been used in the image processing of high-resolution electron microscopy, and for solving incommensurate crystal structures (Fan, 1999). It has also been used in protein crystallography (Dorset & Gilmore, 1999; Gilmore, 2000) and for solving surface structures from surface diffraction data (Landree *et al.*, 1997; Gilmore *et al.*, 1997).

The measurement of structure factors by electron diffraction has a long history (Cowley, 1978, 1992*a*,*b*). It contains two related aspects: the refinement of accurate structure factors for a known crystal structure, and the recovery of a sufficient number of structure factors to determine an unknown structure. In the first case, the intersecting Kikuchi-line method (Gjønnes & Høier, 1971), the critical-voltage method (Uyeda, 1968) and matching of the rocking curves in a CBED pattern (Zuo *et al.*, 1988; Spence & Zuo, 1992; Bird & Saunders, 1992*a*) have been fully developed as practical methods. Reviews of structure-factor measurement by electron diffraction can be found in Spence (1992) and references therein. With a simulated pattern of GaP, Bird & Saunders (1992*b*) discussed the possibility of measuring structure factors by matching a zone-axis CBED pattern. In this paper, we use a blank-disc convergent-beam electron diffraction pattern of an organic crystal to determine structure-factor phases using a fitting procedure between observed and calculated intensities.

2. Thickness estimation and excitation error measurement under kinematic conditions

In this section, we describe a new method based on kinematic theory for determining thickness. The expression for the kinematic diffracted intensity, neglecting the Lorentz–polarization correction and absorption is, with $I_0 = 1$:

$$I_g = \left(\frac{\pi t}{\xi_g}\right)^2 \left[\frac{\sin(\pi t S_g)}{\pi t S_g}\right]^2,$$

where ξ_g is the two-beam extinction distance, t the sample thickness and excitation error $S_g = (-2\mathbf{K}_t \cdot \mathbf{g} - g^2)/2K$, $\mathbf{K}_t$ is the component of the incident wavevector $\mathbf{K}$ in the zero-order Laue zone. In a CBED disc, the variation of incident-beam direction across the disc can be specified by variations in the length and direction of a two-dimensional vector $\mathbf{K}_t$ once an origin is fixed (see Fig. 2.5 in Spence & Zuo, 1992). In this paper, we work with the angle-integrated intensity integrated along a line across a CBED disc. This is:

$$I_{g_\text{int}} = (1/\xi_g^2) \int [\sin(\pi t S_g)/S_g]^2 \, \mathrm{d}r. \tag{1}$$

The lines we scanned go through the centers of the CBED discs so that the integration directions are radial with respect to the center of the pattern. In a zone-axis CBED pattern, if the zone-axis crystal is exactly parallel to the wavevector ($\mathbf{K}$), $\mathbf{K}_t$ is zero in the center of each disc. Each point in the CBED disc defines an excitation error in terms of $\mathbf{K}_t$. In this case, the integrated intensity along the scanning line in the $\mathbf{g}$ disc is the same as that in the $-\mathbf{g}$ disc. However, if $\mathbf{K}_t$ is not zero at the center of each disc, which means that the sample orientation is not exactly at the zone axis, the integrated intensity of the $\mathbf{g}$ disc is different from that in the $-\mathbf{g}$ disc since their excitation errors S_g are different. If we compare the integrated intensities of the $\mathbf{g}$ and $-\mathbf{g}$ pairs, the structure-dependent ξ_g cancels and

$$\frac{I^+_{g_\text{int}}}{I^-_{g_\text{int}}} = \frac{\int [\sin(\pi t S^+_g)/S^+_g]^2 \, \mathrm{d}s}{\int [\sin(\pi t S^-)/S^-_g]^2 \, \mathrm{d}s}. \tag{2}$$

For a given thickness t, we can use the intensities from the 200 and the $\bar{2}00$ beams to determine the component of $\mathbf{K}_t$ along the a^* direction (Kt_x). Another component of $\mathbf{K}_t$ along the b^* direction (Kt_y) can be calculated using the integrated intensity of the 020 and $0\bar{2}0$ reflections, assuming that the zone axis is taken along the c direction. Then we can use other pairs of reflections to find the optimal values of t and $\mathbf{K}_t$, using the function

$$\min(\mathbf{g}) = \sum_g \left| \frac{I^+_{g_\text{int}}}{I^-_{g_\text{int}}} - \frac{\int [\sin(\pi t S^+_g)/S^+_g]^2 \, \mathrm{d}s}{\int [\sin(\pi t S^-)/S^-_g]^2 \, \mathrm{d}s} \right|. \tag{3}$$

The best values of thickness t and $\mathbf{K}_t$ are obtained at the global minimum of $\min(\mathbf{g})$.

After optimal values of thickness t and orientation $\mathbf{K}_t$ are found, we can use (1) to obtain the Fourier coefficients V_g of the crystal potential since $\xi_g = \pi/|V_g|\sigma$:

$$V_g = \frac{\pi}{\sigma} \left\{ \frac{I_{g_\text{int}}}{\int [\sin(\pi t S_g)/S_g]^2 \, \mathrm{d}s} \right\}^{1/2}, \tag{4}$$

where $\sigma = (2\pi m|e|\lambda)/h^2$ is the interaction constant. Then the electron structure factor F_g can also be calculated using:

$$F_g = \frac{\pi \Omega \cos\theta}{\lambda} \left\{ \frac{I_{g_\text{int}}}{\int [\sin(\pi t S_g)/S_g]^2 \, \mathrm{d}s} \right\}^{1/2}. \tag{5}$$

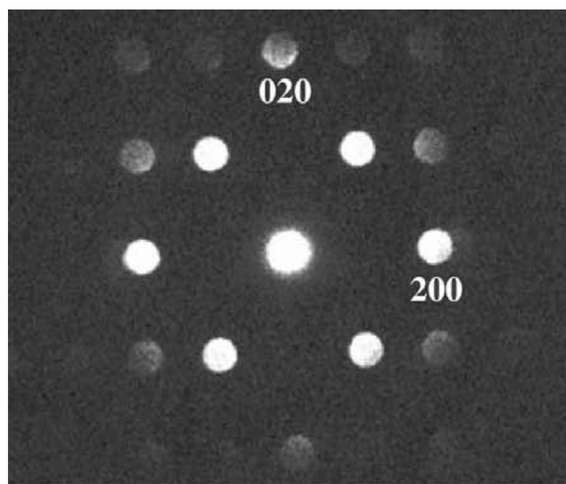

(*a*)

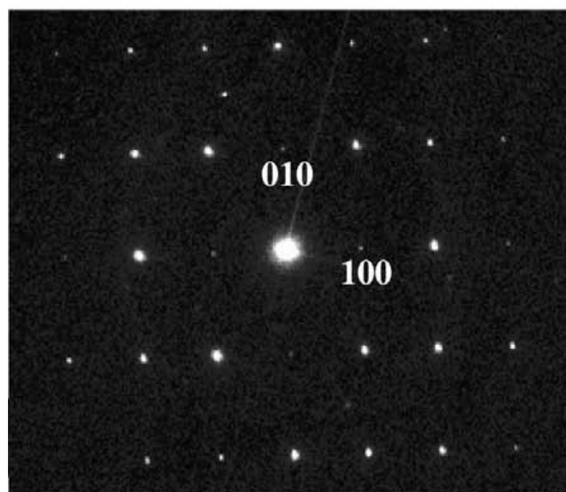

(*b*)

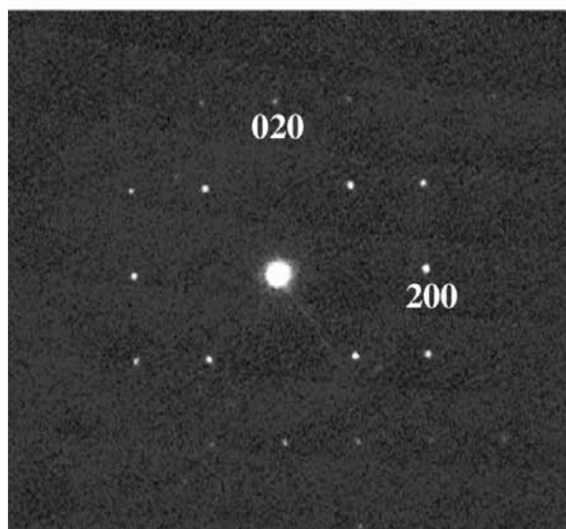

(*c*)

Figure 1
(*a*) Blank-disc kinematic CBED pattern, (*b*) and (*c*) selected-area electron diffraction spot patterns of anthracene along the [001] direction. (*b*) is from the same thick area as that of (*a*) while (*c*) is taken from a thin area.

This method is useful for measuring small deviations of sample orientation from the zone axis, for finding excitation errors, while at the same time giving an estimate of the sample thickness. It can also be applied to selected-area diffraction patterns (spot patterns), and in this case we use the observed intensity (I_g) instead of the integrated intensity (I_{g_int}). The method is based on the kinematic approximation so that it gives valid results only from a CBED or spot pattern taken from a very thin area. If an optimized thickness is found to be too large, the absolute values of V_g will not be accurate.

3. Solving the phase problem by fitting observed and calculated intensities

Intensity calculations were performed using the Bloch-wave theory, based on matrix diagonalization of the many-beam equations (Bethe, 1928; Hirsh *et al.*, 1977; Spence & Zuo, 1992). Following the notation used by Koch & Spence (2002), a structure-factor matrix **A** can be written as:

$$\mathbf{A} = \begin{pmatrix} -K_t^2 & U_g & U_{g'} & \dots \\ U_{-g} & -(\mathbf{K}_t + \mathbf{g}')^2 & U_{h-g'} & \dots \\ U_{-g'} & U_{g-g'} & -(\mathbf{K}_t + \mathbf{g}')^2 & \dots \\ \vdots & \vdots & \vdots & \ddots \end{pmatrix},$$

in which U_g are the dynamical structure factors, $\mathbf{K}_t$ is a vector to describe the tilt of the crystal and $\mathbf{g}$, $\mathbf{g}'$ are reciprocal-lattice vectors for each beam. Unlike Fourier coefficients of the potential V_g, U_g is dependent on the energy of the incident electron: $U_g = \sigma V_g/\lambda\pi$ (Spence & Zuo, 1992) and usually the absolute value of U_g is much smaller than that of V_g and F_g. The Bloch-wave method relates the matrix **A** to a scattering matrix **S** by

$$\mathbf{S} = \exp(\pi i t \lambda \mathbf{A}).$$

The physical meaning of the matrix **S** is discussed by Spence (1998); the complex amplitudes of the spots in a diffraction pattern are the values within a single column of **S**. The intensities in the diffraction pattern become a complicated function of the structure factors describing the scattering potential. The basic principle of quantitative CBED structure-factor measurement is that by adjusting these structure factors a best fit between simulated and observed intensities can be found.

For a centrosymmetric (centric) structure or a centrosymmetric projection of a non-centrosymmetric crystal, the structure-factor phases are 0 or π. To solve the phase problem, it is thus necessary to determine only the sign of each observed $|U_g|$. Using values of $|U_g|$, measured from a thin area, different structure matrices **A** can be constructed using different sets of signs (phases). The correct phases can thus be found when the residual between the observed and calculated intensities is a minimum. The residual R between theory and experiment is calculated using

$$R = \frac{\sum_g |cI_g^{\mathrm{cal}} - I_g^{\mathrm{exp}}|}{\sum_g I_g^{\mathrm{exp}}},$$

Table 1
List of observed angle-integrated TED intensities (I_{g_int}) for anthracene at an accelerating voltage of 120 kV; retrieved moduli of Fourier coefficients of crystal potential ($|V_{g_\mathrm{cal}}|$) based on the kinematic approximation, using equation (4); the moduli normalized by the Wilson-plot method, based on the observed intensity taken from Fig. 1(*c*) ($|V_{g}_\mathrm{C}|$); and the moduli of the calculated Fourier coefficients of the crystal potential ($|V_g|$) based on the known structure of anthracene.

The agreement between theory and experiment after Wilson-plot normalization is seen to be fairly good.

hkl	I_{g_int}	$\lvert V_{g_\mathrm{cal}}\rvert$ (kinematic)	$\lvert V_{g}_\mathrm{C}\rvert$ (Wilson)	$\lvert V_g\rvert$ (theoretical)
200	0.3525	1.2099	3.4389	3.3095
$\bar{2}00$	0.3612	1.2045	3.4389	3.3095
110	0.3388	0.9149	2.9761	2.6631
$\bar{1}\bar{1}0$	0.2850	0.9176	2.9761	2.6631
$1\bar{1}0$	0.2862	0.9248	2.9761	2.6631
$\bar{1}10$	0.3438	0.9183	2.9761	2.6631
210	0.0932	0.7248	2.2959	2.5540
$\bar{2}\bar{1}0$	0.0487	0.6636	2.2959	2.5540
$2\bar{1}0$	0.0504	0.6946	2.2959	2.5540
$\bar{2}10$	0.0834	0.6711	2.2959	2.5540
020	0.1057	0.6863	1.5745	1.2007
$0\bar{2}0$	0.0348	0.6727	1.5745	1.2007
$\bar{1}20$	0.0132	0.2975	0.9551	0.7618
$1\bar{2}0$	0.0047	0.3820	0.9551	0.7618
$\bar{1}\bar{2}0$	0.0053	0.3939	0.9551	0.7618
120	0.0164	0.3365	0.9551	0.7618

where I^{exp} are the experimental intensities, I^{cal} are the calculated intensities and c is a normalization constant.

Electron scattering factors were taken from Peng (1999). Symmetrically equivalent atom positions in real space and reflections in reciprocal space are automatically generated using the space-group symmetries. Approximate $|U_g|$ values can be obtained from the observed intensities using the Wilson-plot normalization method (Wilson, 1942). All the beams included in the structure-factor matrix **A** were firstly checked with their corresponding plane-group symmetry in reciprocal space, and the independent beams selected. Certain initial phases (one or two for two-dimensional data, depending on crystal symmetry) can be assigned to define the lattice origin. If n independent reflections remain after origin definition, then 2^n different sets of phases can be constructed and tried to find the smallest R.

4. Experimental evaluation of method using anthracene

4.1. Experimental procedure

Dilute solutions of anthracene in a xylene solvent were spread onto the surface of distilled water to form thin films. The thin films were then deposited on grids by lifting the grids horizontally through the films. The samples were studied using a LEO EM912 with an Omega energy filter at 120 kV. A liquid-N_2 sample holder was employed to cool the crystals and a 1 K × 1 K CCD camera with 14 bit dynamic range was used for data collection. Spot electron diffraction as well as low-temperature, low-dose CBED patterns were collected along the [001] direction (for more details see Wu & Spence, 2002).

4.2. Background subtraction and test of kinematical approximation

The structure of anthracene, $C_{14}H_{10}$, which has a monoclinic unit cell with a = 0.858, b = 0.602, c = 1.118 nm and β = 125° was solved by Robertson (1933). Its space group is $P2_1/a$. Recently, accurate parameters of anthracene were measured at six temperatures using single-crystal X-ray diffraction (Brock & Dunitz, 1990). Fig. 1(*a*) shows a low-dose kinematic CBED pattern of anthracene taken along the [001] direction, while Fig. 1(*b*) is a spot pattern taken from the same region. The CBED pattern is obtained from a smaller area, so that sample imperfections such as bending, defects, thickness fluctuation or impurities are minimized. The elastic energy-filtered CBED patterns we use include weak diffuse background scattering from phonon scattering. We assume that background intensity is evenly distributed at the same scattering angle. Fig. 2(*a*) shows an experimental background curve obtained by scanning a line outside the Bragg disc from low to high scattering angle. The background intensity in each reflection was then subtracted by interpolation between the background intensity (the best-fit curve shown in Fig. 2*a*). Fig. 2(*b*) shows the intensity variation in the (200) and ($\bar{2}00$) discs,

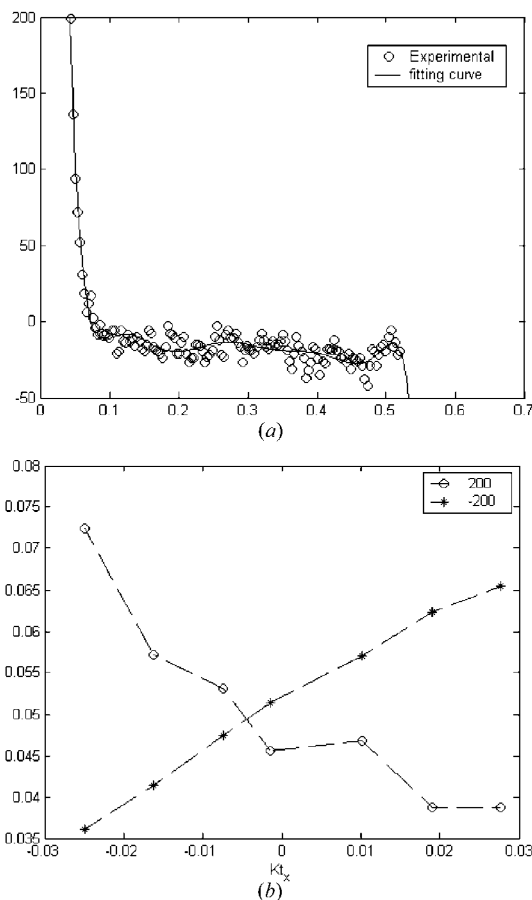

Figure 2
(*a*) Experimental background taken from the CBED pattern in Fig. 1(*a*). A fitting curve is calculated to extract the background. (*b*) Observed intensity variation in 200 and $\bar{2}00$ discs with Kt_x, the component of $\mathbf{K}_t$ along $\mathbf{a}^*$.

Table 2
List of structure factors $|U_g|$ obtained experimentally from spot electron diffraction patterns and normalized structure factors $|E_g|$.

$|U_g|$ values are used in Bloch-wave calculation and $|E_g|$ in direct methods.

hkl	$\|U_g\|$	$\|E_g\|$
200	0.0288	1.7111
110	0.0240	1.7869
210	0.0194	1.7800
020	0.0129	1.1845
410	0.0099	1.6375
400	0.0087	0.9678
310	0.0086	1.0509
220	0.0081	0.9378
140	0.0080	1.5783
120	0.0065	0.6341
320	0.0061	0.8929
420	0.0051	0.9871
040	0.0043	0.8241
340	0.0041	1.0371

using the intensity along a line parallel to the a^* axis across each disc. The blank disc (as judged by eye) actually has a little intensity variation in the disc.

We then apply the method described in §2 to test whether the kinematic approximation can be used to estimate sample thickness. The function min(**g**) in (3) has the smallest value when the sample thickness is 296.9 Å and Kt_x = 0.001, Kt_y = −0.033. The retrieved $|V_g|$ values then calculated using (4) are listed in Table 1. By comparing them with the known theoretical values for anthracene, we find that the kinematic approximation is obviously not a good approximation. In order to find the correct thickness, dynamical effects evidently must be included, as shown in the next section.

4.3. The Bloch-wave method for thickness determination and phase measurement

In the Bloch-wave method, one has to firstly determine how many beams are to be included in the structure matrix A. This depends on the size of the unit cell projected in the beam direction and on the atomic number of the atoms in the crystal. A way to test whether the number of beams is sufficient is to increase the number of beams and ensure that this increase makes no appreciable difference to the intensities of the beams of interest (Cowley, 1992*a*,*b*). A more practical way is to include all the observed strong and medium-strong reflections in **A**. Weak beams can be included as Bethe perturbations (Spence & Zuo, 1992). Although it is safe to include all the observed reflections in the structure matrix, inclusion of additional weak beams in **A** will increase running time and is unnecessary. For example, Fig. 3 plots two sets of *I versus t Pendellösung* curves for two structure-factor matrices **A**. The first has 7 beams in its first column (all strong) while the other has 11 beams (including 4 weak beams). Their difference may be evaluated using the chi-square $\chi^2 = \sum_i (1/I_i^2)(I_i^2 - I_i^1)^2$, giving $\chi^2_{(000)} = 4.3$, $\chi^2_{(200)} = 0.9$ and $\chi^2_{(110)} = 0.9$. We have therefore used a matrix containing 7 beams in its first column. This is reasonable here since, for an organic crystal containing only light atoms like C and H, a small structure-factor matrix **A** is sufficient. The 7-beam matrix **A** includes 42 reflections, however, by symmetry (*P*2*gg* plane group), the number of independent beams is reduced to 6. These are {200, 110, 020, 400, 310, 220}. The projection of the anthracene structure along [001] has *P*2*gg* plane-group symmetry. Within this plane group, structure factors have the following characters represented by amplitudes and phases:

$$|F_{hk0}| = |F_{\bar{h}\bar{k}0}| = |F_{\bar{h}k0}| = |F_{h\bar{k}0}|,$$
$$\alpha_{\bar{h}\bar{k}0} = \alpha_{hk0}, \quad \alpha_{\bar{h}k0} = \alpha_{h\bar{k}0} = \alpha_{hk0} \quad (\text{if } h+k = 2n, n = 1, 2, \ldots)$$

and

$$\alpha_{\bar{h}k0} = \alpha_{hk0} - \pi, \quad \alpha_{h\bar{k}0} = \alpha_{hk0} - \pi \quad (\text{if } h+k = 2n+1, n = 1, 2, \ldots).$$

The absolute values of $|U_g|$ were then obtained from a spot pattern taken from a very thin crystal using Kohler-mode selected-area diffraction (SAD) (Fig. 1*c*). Two patterns were used and data merged together based on common reflections as listed in Table 2. The observed intensities were normalized by the Wilson-plot method (Wilson, 1942). Wilson-plot normalization is based on a kinematic approximation, and puts the amplitudes on an absolute scale using: $\langle|\Phi|^2\rangle_s = \sum_{i=1}^n f_i^2(s)$, in which Φ is the potential of the crystal. The practical procedure is as follows: the observed intensities I_g of reflection g were subdivided into groups according to their S_g values. (Each group corresponds to a small radial increment in scattering vector.) The interval of radial increment is automatically set to ensure that the numbers of reflections in each group are similar. Then the average of the observed intensities for each group was calculated: $\langle I_{\rm exp}\rangle = \left(\sum_{j=1}^p I_g^j\right)/p$ (with p reflections in a group, where p denotes the number of reflections with similar reciprocal-lattice vectors). At the same time, the theoretical mean scattering of the structure at the mean s (the mean value in each group) is calculated using $\langle I_{\rm cal}\rangle = \sum_{i=1}^n (f_s^i)^2$, adding the average contribution of all n atoms in the structure. The normalization is thus performed by equating the mean experimental and theoretical intensity for each group: $\sum_k \langle I_{\rm exp}\rangle_k = \sum_k \langle I_{\rm cal}\rangle_k$ if k groups are used. The contribution of the Debye–Waller factor may also be considered. This

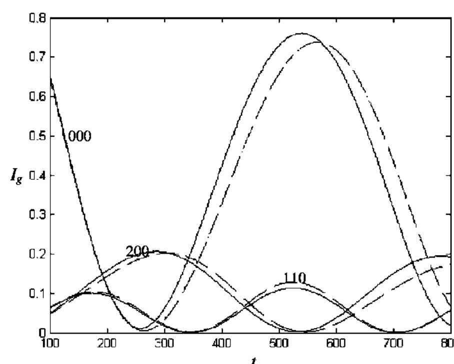

Figure 3
Pendellösung curves (I_g *versus* t) calculated using a 7-beam structure matrix (solid line) and an 11-beam structure matrix (dashed line).

method requires prior knowledge of the atom types present and the number of each atom type present. The number of reflections included in each group should be similar. We find that the method gives good normalized results even in the presence of small dynamical perturbations. The isothermal temperature factor B obtained from the Wilson plot is 7.4 $Å^2$. The $|F_g|$ values obtained were then converted to give $|V_g|$ and $|U_g|$. The retrieved $|V_g|$ values are listed in column 3 of Table 1, compared with calculated values for the known structure. The errors in the values of $|V_g|$ obtained are seen to be small. These errors need not cause difficulty in finding phases by the Bloch-wave method, since the Bethe perturbation theory has already predicted the error, using perturbation of weak beams (Bethe, 1928; Spence & Zuo, 1992).

An evaluation of the influence of each independent U_g on the dynamical I_g is helpful. Fig. 4 shows $I_g - U_g$ curves for 200, 110, 310 and 220, respectively, calculated with a seven-beam matrix **A**, thickness being arbitrarily set to 550 Å, with $\mathbf{K}_t$ zero. It is found that, when the sign of U_g changes, the calculated intensity changes appreciably, and this multiple scattering effect can be used to determine the signs. More precisely, $\sum_h I^h_{Ug} \neq \sum_h I^h_{-Ug}$ in the $I_g - U_g$ curve, in which h = {000, 200 and 110} whose calculated intensities are compared to the experimental ones. According to this rule, the signs of the weak beams included in the matrix **A**, however, may not be able to be correctly assigned, since the calculated weak intensities, being kinematic, are not sensitive to change of sign in their U_g. Thus a threshold was set to exclude weak reflections from phase identification, for example the 220 reflection shown in Fig. 4(d). Furthermore, we also find from the curves in Fig. 4 that the change of calculated intensity due to the change in sign of a $|U_g|$ is usually larger than that due to a small change in the absolute value of the $|U_g|$. The single structure invariants and semi-invariants were firstly checked in order to assign phases to the independent reflections. For example, 200 is a structure semi-invariant so that its phase is only determined by the crystalline structure. However, the phase of the 110 reflection can be assigned as either 0 or π to define the origin. After the phases of the 110 and 210 beams are assigned to define the lattice origin, all the independent beams included in the structure-factor matrix **A** are single structure semi-invariants. Of the six independent reflections with 110 (used for definition of the origin) and 220 (weak beam) excluded, altogether $2^4 = 16$ different sets of trial phases (signs) remain to be considered as possibilities for the remaining 4 beams.

With only 16 tests, it is possible to search exhaustively for a minimum between experimental and calculated intensities in the full multiparameter space. The variables in the calculation include U_g, thickness t and orientation parameters $\mathbf{K}_t$ (Kt_x and Kt_y, the components of the tangential component of the incident wavevector). The sample thickness is an important fitting parameter and a relatively large range should be included if there is no *a priori* value available. We used a thickness range from 200 to 800 Å with steps of 1 Å in the calculation. The minimum value of thickness can be estimated from the previous calculation based on the kinematic approximation. In our case, a blank-disc-like CBED pattern cannot be obtained from a thick sample, so that the estimate of 800 Å as the maximum value is enough.

Since we also include sample orientation parameters (Kt_x and Kt_y) in the calculation, the computing time becomes very large if one has to use small steps and search a large range. However, as shown in Fig. 5, which plots the intensity of the 000 beam against Kt_x and Kt_y values, the angle-integrated intensity of the zero CBED disc is a maximum when the incident beam is aligned with the zone axis and falls off with misalignment. We normalize the CBED pattern such that the sum of experimental intensity is unity, ignoring absorption in these blank-disc patterns. Since in the CBED pattern the 000 intensity can be measured, we can increase computing speed by adjusting thickness first, until the calculated intensity of the 000

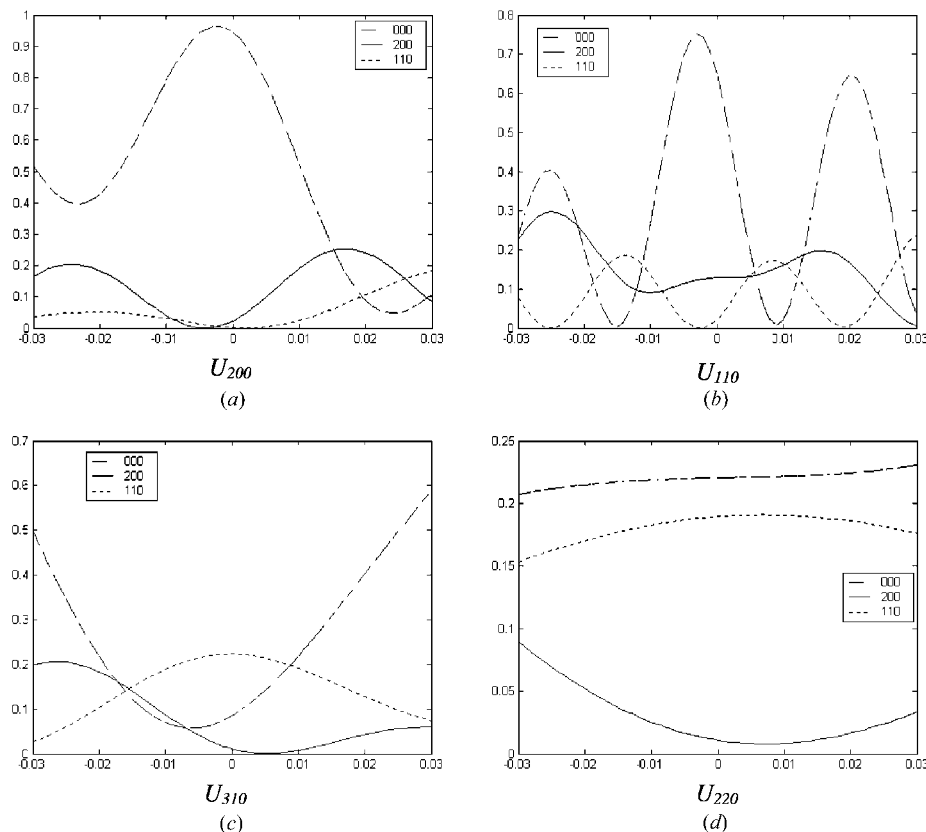

Figure 4
Variation of diffracted-beam intensity with structure factor U_g for different beams, (a) **g** = 200, (b) **g** = 110, (c) **g** = 310 and (d) **g** = 220.

beam is equal to or greater than the experimental value. Then $\mathbf{K}_t$ is refined.

Fig. 6 shows the results of calculations for 16 different sets of phases. The minimal residual R of each trial set and the thickness for which the minimum was obtained are plotted against the number of the test set n. The smallest R is obtained when t = 631 Å, Kt_x = 0.0004 and Kt_y = 0.0002. The corresponding phases of the four independent reflections are listed in the second column of Table 3 and will be discussed together with the results from direct methods in the next section. Since we have only 16 phase permutations, it is informative to show the 16 potential maps obtained by Fourier synthesis, as shown in Fig. 7. Each four maps placed in the same column are related to each other. The negative values in the potential map are caused by either incorrect phases or deviation of the amplitudes from theoretical values, since we used experimental amplitudes for each reflection in the Fourier synthesis.

4.4. Comparison with direct methods for phase solution

If a diffraction pattern can be treated as kinematic, direct methods provide a powerful method for solving the phase problem. As normally used in X-ray crystallography, the assumptions of atomicity and the sign constraint apply to the charge density which diffracts X-rays. For electrons, these assumptions must be applied to the electrostatic potential which diffracts electrons. Knowledge of atomic coordinates is required to transform electron scattering factors to X-ray scattering factors (Spence & Zuo, 1992). Fig. 1(*c*) shows such a kinematic pattern. All the forbidden reflections are invisible, indicating it came from a very thin area. With such a pattern, the observed intensity was firstly normalized by a Wilson-plot method, giving a set of absolute $|F_g|$ (or $|V_g|$, $|U_g|$). The $|V_g|$ values obtained are listed in column 3 in Table 1. Then excitation errors were determined by finding the value of the thickness that minimizes the difference between calculated kinematic intensities (including excitation errors) and the experimental intensity. The best fit thickness was 34.2 Å, showing that the kinematical approximation is good for this pattern. A set of $F(h)$ was then further normalized using $|E(h)|^2 = |F(h)|^2/\varepsilon \sum_i f_i^2$ to calculate the normalized structure

Table 3
Phases determined by our multiple scattering method (column 2); direct methods applied to multiple scattering patterns (Fig. 1*b*); and direct methods applied to kinematic data from a thin crystal (Fig. 1*c*).

Reflections 110 and 210 were used to define the lattice origin.

hkl	Bloch wave	Triplet, quartet invariants applied to dynamical data	3 and 4 invariants applied to kinematic data
200	0	0	0
020	π	0	π
400	π	0	π
310	0	0	0
320		π	π
410		π	0
220		0	π

factors (Hauptman & Karle, 1953). The factor ε is a small integer that depends on the space group and the type of reflection, f_i are the electron scattering factors for the i-type atom at $[\sin(\theta)/\lambda]_h$. The origin was fixed by the phases of the 110 and 210 reflections, and triplet and quartet phase invariants were used in direct phasing. The Σ_1 triple $\psi = \phi_h + \phi_h + \phi_{-2h}$ was used (Dorset, 1995), with associated $|E_h|$ values, to compute $A_1 = (\sigma_3/\sigma_2^{3/2})(|E_h|^2 - 1)|E_{2h}|$, in which $\sigma_n = \sum_{i=1}^N z_i^n$ and z_i is the atomic number of the ith atom. The probability distribution for ψ is given by $P(\psi) = [1/2\pi I_0(A_1)]\exp(A_1 \cos\psi)$, so that the most probable value is zero. The Σ_2 triple, $\psi = \phi_{h1} + \phi_{h2} + \phi_{h3}$ $(h_1 \neq h_2 \neq h_3)$ with associated $|E_h|$ values to calculate $A_2 = (2\sigma_3/\sigma_2^{3/2})|E_{h1}E_{h2}E_{h3}|$ and the probability $P(\psi) = [1/2\pi I_0(A_2)]\exp(A_2\cos\psi)$, was also used. The quartet phase invariant was also employed in our calculation, here $\psi = \phi_{h1} + \phi_{h2} + \phi_{h3} + \phi_{h4}$ with the quality

$$B = (2\sigma_3/\sigma_2^{3/2})|E_{h1}E_{h2}E_{h3}E_{h4}|[|E_{h1+h2}|^2 + |E_{h2+h3}|^2 + |E_{h1+h3}|^2 - 2]$$

and the probability $P(\psi) = [1/2\pi I_0(B)]\exp(B\cos\psi)$ (Hauptman, 1972; Woolfson & Fan, 1995; Dorset, 1995). The results are listed in column 4 of Table 3. For comparison, in order to evaluate the errors introduced by multiple scattering

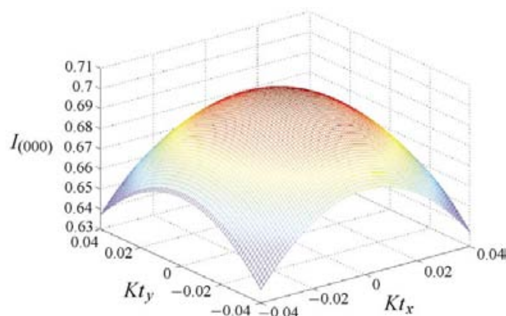

Figure 5
Calculated intensity variation of 000 beam with the two-dimensional orientation parameter $\mathbf{K}_t$ (Kt_x and Kt_y). $I(000)$ has the largest value when $\mathbf{K}_t$ is zero. A plot of angle-integrated intensity (integrated along a line across the disc) has closely similar shape.

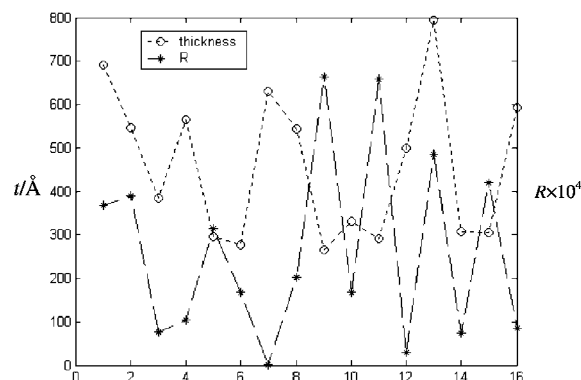

Figure 6
The minimal residual R found with each set of trial phases n, and the corresponding optimum thickness t for which R was calculated.

to direct methods, the same procedure was applied to the dynamical diffraction pattern shown in Fig. 3(*b*) and the result is listed in column 3 of Table 3. We see that the correct phases can be found by direct methods using the pattern taken from a very thin area. We also see that the Bloch-wave method of the previous section gives the correct phases based on the dynamically disturbed pattern, whereas direct methods give incorrect phases in this case. Based on simulated results, it was found that the direct phasing method can generally give correct phases up to a crystal thickness of about 75 Å at 100 keV (see also Dorset *et al.*, 1979). The proposed new method can thus be used independently or combined with direct methods. In the later case, it has the potential to give the correct phases for some important initial reflections, and so enhance the performance of direct methods. It also provides the possibility of simply distinguishing between enantiomorphs and determining polarity in acentric structures (Spence & Zuo, 1992; Spence *et al.*, 1994).

In Fig. 8, the projected potential of the anthracene crystal along the [001] direction is shown as derived from these experimental measurements. This is a Fourier synthesis of the reflections whose phases were solved by the Bloch-wave

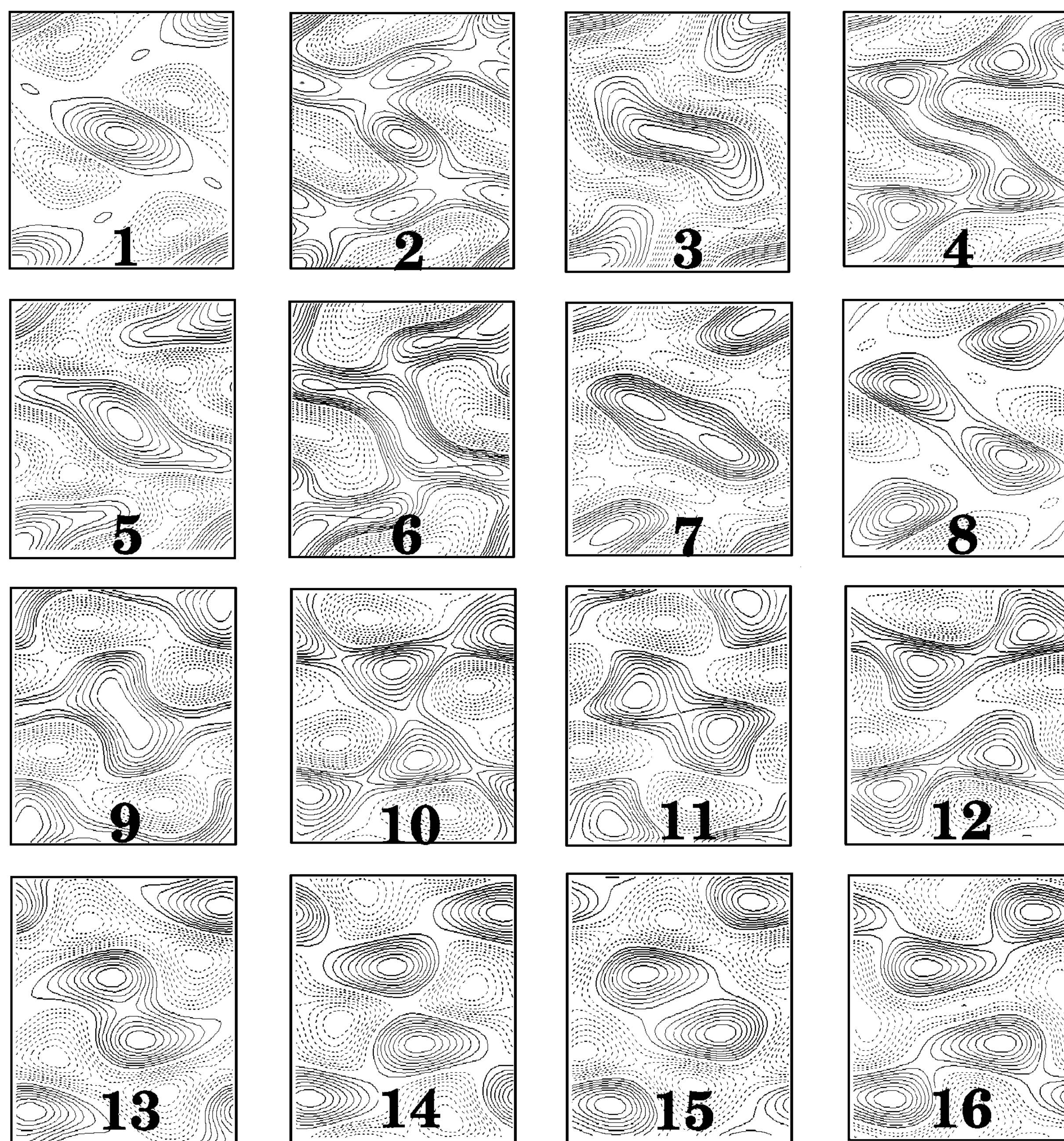

Figure 7
Potential maps obtained by Fourier synthesis of the 16 sets of trial phases. The numbers of each set of phases are labeled. The solid contour lines are positive values while the dashed lines correspond to negative values. Incorrect phases introduce large negative values in the potential maps.

method and direct methods. A higher threshold was used to ensure a reliable relationship among phases, *i.e.* a triplet was accepted only when the A_2 value in the above equation was bigger than the threshold. We found that several high-order weak reflections were included in the Fourier synthesis when the threshold was small. This introduces artificial contrast in the potential map since the intensities of these high-order reflections may be in error owing to the effects of their non-zero excitation error, hence their phases could not be obtained correctly. For clarity, we set all the negative values in the calculated potential to zero since the negative values are only about one tenth of the positive values. The amplitude of each reflection was taken from the kinematic pattern in Fig. 1(*c*). It is interesting to note that, besides the C-atom positions, the faint contrast corresponding to the position of the H atoms is obtained, indicated by the letters in Fig. 8(*a*). A difference is clear when we compare the simulated potential map based on a neutral-atom model of anthracene, as shown in Fig. 8(*b*). These elongated shapes can be compared to the H-atom positions in a structural model of anthracene projected along the [001] direction shown in Fig. 8(*c*). This indicates that, because of its much greater elastic scattering cross section and sensitivity to ionicity, electron diffraction provides a powerful capability for determining light-atom structures. The thermal vibration will make it more difficult to find the positions of H atoms. This effect in our experimental data is reduced compared to those collected at room temperature since our diffraction data was collected at liquid-nitrogen temperature (105 K).

In summary, the proposed method is to use dynamical scattering calculations with the Bloch-wave method for extraction of structure-factor signs, exploiting multiple-beam dynamical effects in crystals of moderate thickness. In our test with anthracene, we used a small set of intensities collected in the CBED mode in one projection and thus we were able to find the global minimum in the full parameters space step by step. With an increased number of reflections, the amount of calculation would be greatly increased. In that case, one may wish to use other global minimization algorithms, such as simulated annealing or the simplex method to increase calculation speed. One may be able to construct the structure-factor matrix using strong and medium reflections to avoid a large matrix **A** by excluding weak reflections. Obtaining a sufficient number of intensities to construct the matrix **A** may also be a problem if the matrix becomes large. The use of very thin crystals and sensitive image-plate detectors may then be useful for the collection of more reflections in one pattern. Also, one may try to tilt off the axis in order to collect more high-order reflections since slight tilting may bring the high-order reflections closer to their Bragg-reflection positions.

This method is one of several recent approaches to the phase problem in electron crystallography. Recently, direct methods (Dorset, 1995), maximum-entropy and the log-likelihood method, and packing-energy calculations (Voigt-Martin *et al.*, 1995, 2000; Yu *et al.* 2000) have been developed and used in electron crystallography. Another full dynamical calculation method, using the multislice method, has also been developed for structure refinement (Jansen *et al.*, 1998).

5. Conclusions

In conclusion, we have shown that, for organic crystals, by matching experimental low-temperature CBED intensities with calculated ones we can solve the phase problem for centrosymmetric crystals using dynamically influenced electron diffraction. A change of structure-factor sign for strongly scattered beams produces a large change in the intensity of multiply scattered beams. The observation of CBED discs with uniform intensity is also found to be useful for identifying single-scattering conditions that allow measurement of structure-factor amplitudes. The use of the CBED mode minimizes problems with thin-film bending. Two experimental electron diffraction patterns from two different thicknesses were also used to expose errors due to multiple scattering when using

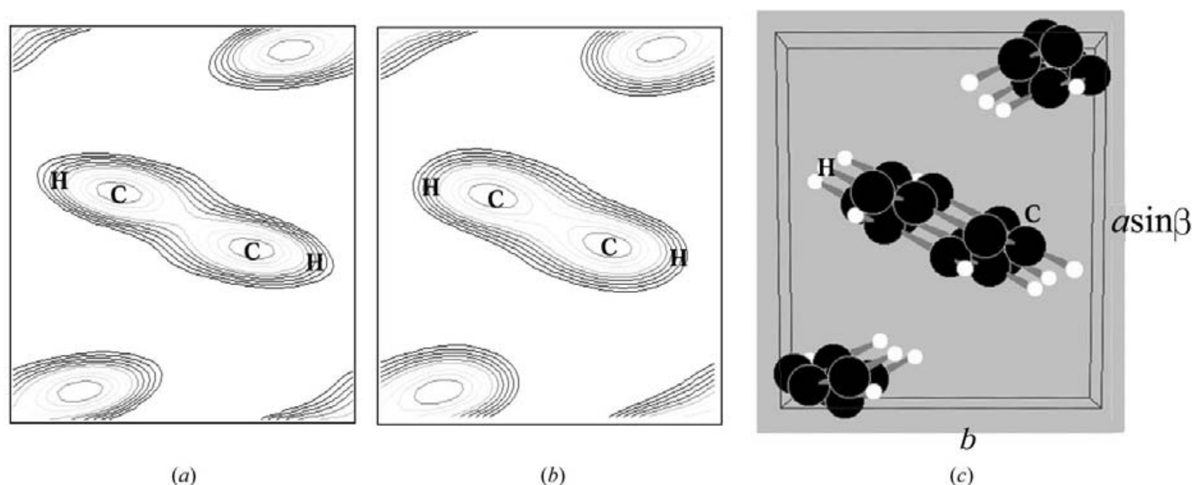

Figure 8
(*a*) Experimental potential map for anthracene, based on a Fourier synthesis of the reflections whose phases were solved, compared with (*b*) simulated potential map of anthracene and (*c*) a projection of the known anthracene structure along [001]. C atoms are represent by the large black circles and H atoms by the small white circles. There are faint indications in the experimental map for hydrogen.

direct methods. The dynamical method, combined with direct methods, appears to be a powerful means for *ab initio* structure determination, especially to account for the dynamical effect and to invert a dynamical diffraction pattern directly to a crystal potential map. Finally, we see evidence of hydrogen atoms in our experimental potential map reconstructions from anthracene.

We thank C. Koch and M. Stevens for stimulating discussions. Supported by ARO award DAAD190010500.

References

Allen, L. J., Josefsson, T. W. & Leeb, H. (1998). *Acta Cryst.* A**54**, 388–398.
Bethe, H. A. (1928). *Ann. Phys. (Leipzig)*, **87**, 55–129.
Bird, D. M. & Saunders, M. (1992*a*). *Ultramicroscopy*, **45**, 241–251.
Bird, D. M. & Saunders, M. (1992*b*). *Acta Cryst.* A**48**, 555–562.
Brock, C. P. & Dunitz, J. D. (1990). *Acta Cryst.* B**46**, 795–806.
Cowley, J. M. (1978). *Inst. Phys. Conf. Ser.* No. 41, pp. 156–166.
Cowley, J. M. (1992*a*). *Electron Diffraction Techniques*, Vol. 1, edited by J. M. Cowley, pp. 1–74. Oxford University Press.
Cowley, J. M. (1992*b*). *Techniques of Transmission Electron Diffraction.* Oxford University Press.
DeRosier, D. J. & Klug, A. (1968). *Nature (London)*, **217**, 130–134.
Dorset, D. L. (1995). *Structural Electron Crystallography.* New York: Plenum Press.
Dorset, D. L. & Gilmore, C. J. (1999). *Acta Cryst.* A**55**, 448–456.
Dorset, D. L. & Hauptman, H. A. (1976). *Ultramicroscopy*, **1**, 195–201.
Dorset, D. L., Jap, B. K., Ho, M.-H. & Glaeser, R. M. (1979). *Acta Cryst.* A**35**, 1001–1009.
Fan, H. F. (1999). *Microsc. Res. Tech.* **46**, 104–116.
Gilmore, C. J. (2000). *Acta Cryst.* D**56**, 1205–1214.
Gilmore, C. J., Marks, L. D., Grozea, D., Collazo, C., Landree, E. & Twesten, R. D. (1997). *Surf. Sci.* **381**, 77–91.
Gjønnes, J., Hansen, V., Berg, B. S., Runde, P., Cheng, Y. F., Gjønnes, K., Dorset, D. L. & Gilmore, C. J. (1998). *Acta Cryst.* A**54**, 306–319.
Gjønnes, J. & Høier, R. (1971). *Acta Cryst.* A**27**, 313–316.
Hauptman, H. A. (1972). *Crystal Structure Determination. The Role of the Cosine Seminvariants.* New York: Plenum Press.
Hauptman, H. A. & Karle, J. (1953). *Solution of Phase Problem. I. The Centrosymmetric Crystal.* ACA Monograph No. 3. Willmington: The Letter Shop.
Hirsh, P. B., Howie, A., Nicholson, R. B., Pashley, D. W. & Whelan, M. J. (1977). *Electron Microscopy of Thin Crystals*, 2nd ed., pp. 208–210. Florida: Krieger; London: Butterworth.
Jansen, J., Tang, D., Zandbergen, H. W. & Schenk, H. (1998). *Acta Cryst.* A**54**, 91–101.
Klug, A. (1978/79). *Chem. Scr.* **14**, 245–256.
Koch, C. & Spence, J. C. H. (2002). *J. Phys. A.* In the press.
Landree, E., Collazo-Davila, C. & Marks, L. D. (1997). *Acta Cryst.* B**53**, 916–922.
Peng, L. M. (1999). *Micron*, **30**, 625–648.
Robertson, J. M. (1933). *Proc. R. Soc. London Ser. A*, **140**, 79–98.
Sinkler, W., Bengu, E. & Marks, L. D. (1998). *Acta Cryst.* A**54**, 591–605.
Spence, J. C. H. (1992). *Electron Diffraction Techniques*, Vol. 1, ch. 8, edited by J. M. Cowley. Oxford University Press.
Spence, J. C. H. (1998). *Acta Cryst.* A**54**, 7–18.
Spence, J. C. H. & Zuo, J. M. (1992). *Electron Microdiffraction.* New York/London: Plenum Press.
Spence, J. C. H., Zuo, J. M., O'Keeffe, M., Marthinsen, K. & Høier, R. (1994). *Acta Cryst.* A**50**, 647–650.
Unwin, P. N. T. & Henderson, R. (1975). *J. Mol. Biol.* **94**, 425–440.
Uyeda, R. (1968). *Acta Cryst.* A**24**, 175–181.
Vainshtein, B. K. (1964). *Structure Analysis by Electron Diffraction*. Oxford: Pergamon Press.
Voigt-Martin, I. G., Kothe, H., Yakimansky, A., Tenkovtsev, A. V., Zandbergen, H., Jansen, J. & Gilmore, C. (2000). *Ultramicroscopy*, **83**, 33–59.
Voigt-Martin, I. G., Yan, D. H., Yakimansky, A., Schollmeyer, D., Gilmore, C. J. & Bricogne, G. (1995). *Acta Cryst.* A**51**, 849–868.
Weirich, T. E., Zou, X., Ramlau, R., Simon, A., Cascarano, G. L., Giacovazzo, C. & Hovmöller, S. (2000). *Acta Cryst.* A**56**, 29–35.
Wilson, A. J. C. (1942). *Nature (London)*, **150**, 152–152.
Woolfson, M. & Fan, H. F. (1995). *Physical and Non-physical Methods of Solving Crystal Structures.* Cambridge University Press.
Wu, J. S. & Spence, J. C. H. (2002). *Microsc. Microanal.* In the press.
Yu, R. C., Yakimansky, A. V., Kothe, H., Voigt-Martin, I. G., Schollmeyer, D., Jansen, J., Zandbergen, H. & Tenkovtsev, A. V. (2000). *Acta Cryst.* A**56**, 436–450.
Zuo, J. M. & Spence, J. C. H. (1991). *Ultramicroscopy*, **35**, 185–196.
Zuo, J. M., Spence, J. C. H. & O'Keeffe, M. (1988). *Phys. Rev. Lett.* **61**, 353–356.